# A pseudoelastic model for deformation twinning: Numerical homogenisation and comparison to experiments

# Rainer Glüge\*

Otto-von-Guericke-Universität Magdeburg, Universitätsplatz 2, D-39106.

# Abstract

A pseudoelastic micromodel that accounts for deformation twinning and crystallographic slip (Glüge *et al.*, 2010) is used in conjunction with the representative volume element (RVE) method. The material model consists basically of a nonconvex visco-elastic stress strain-relation, and has to be considered as a microscale-model. The material parameters are adopted to  $\{10\overline{1}2\}\langle\overline{1}011\rangle$  twinning in magnesium. The simulation setup follows the commonly conducted compression tests on extruded Magnesium rods, where due to twinning a strong change of texture and a strength differential effect can be observed. The simulations allow for an investigation of the twin propagation in the polycrystal. Furthermore, the simulated twin volume fraction evolution, the texture evolution and the macroscopic stress-strain relation could be compared to experimental findings obtained with pure magnesium and the magnesium based alloy AM30.

Key words:  $\{10\bar{1}2\}\langle\bar{1}011\rangle$  twinning, pseudoelasticity, nonconvex strain energy, magnesium, crystal plasticity, homogenisation, representative volume element technique, texture, strength differential effect

# 1. Introduction

Many materials undergo solid to solid phase changes upon thermal or mechanical loading, which results in phenomena like the shape memory effect (SMA), the transformation induced plasticity effect (TRIP) or the twinning induced plasticity effect (TWIP). In this work, the focus is on the isothermal and mechanically induced deformation twinning. The twins develop as small layers. On the grain scale, these layers display a homogeneous shear deformation with a specific amount of shear, while on the atomic scale, one observes a long-range reordering of the atomic lattice, such that a rotated copy of the parent lattice is generated. For shuffle-free twinning modes, the twin lattice is obtained by applying a homogeneous shear deformation to the parent lattice, while for twinning modes including shuffling, the homogeneous shear deformation leaves only the atoms of a sub-lattice in their proper twin configuration, while the remaining atoms undergo a shuffling displacement (Christian and Mahajan, 1995), see Figure 1. In both cases, a regular reordering of the atomic bonding is observed. Although from a chemical point of view one might not want to speak about a phase change, some characteristic ingredients of phase changes are displayed. Twinning produces sharp interfaces, at which the material properties that depend on the crystal orientation undergo a jump. The twins form as plates inside of grains, and can alter significantly the morphological and the crystallographic texture, both influencing the yield behaviour and the elastic anisotropy. Due to its polarity, twinning can cause a pronounced differential effect on the strength of the material and the forming limit. For many materials, these effects are not negligible, and need to be incorporated in the material model. Especially the ductile TWIP steels and the lightweight hcp metals magnesium and titanium, which are interesting for engineering applications, display

<sup>\*</sup>Corresponding author. Email: gluege@ovgu.de

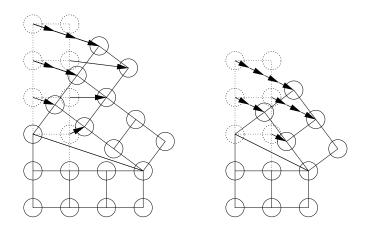


Figure 1: A twinning mode involving shuffling and a shuffle-free twinning mode.

extensive twin formation at room temperature. For such materials, the proper prediction of forming processes requires a material model which includes mechanical twinning.

One approach, proposed by Ericksen (1975, 1984), is to treat phase changes by a non-convex elastostatic modelling. Let w denote the elastic strain energy and E be the strain measure. Then, the overall modelling strategy is to construct an elastic strain energy w(E) which exhibits nonconvex regions. In this regions, no stable equilibrium state can be attained. The convex branches are assigned to different phases, which are separated by the nonconvex regions. This leads to the pseudoelastic boundary value problem. The latter is ill-posed, since generally no unique energy-minimising configuration can be given. Different strategies to overcome the ill-posedness have been proposed, which can be roughly classified into relaxation and kinetisation.

Some work has been contributed to the energy relaxation strategies, initialised by introducing different notions of convexity (Ball, 1977). One way of relaxing w(E) is to replace it by a convexified strain energy  $w_c(E)$ .  $w_c(E)$  should reproduce the main features of w(E). For an analytical relaxation, often several simplifications (small strains, elastic isotropy, two-well potential) are needed (Govindjee *et al.*, 2003), and in general no analytical solution may be attained. Since an exact quasiconvexification is only possible in rare cases, it needs to be approximated in terms of bounds, i.e. by the rank-1-convex and the polyconvex hull. For this purpose, numerical relaxation schemes have been developed (Pagano *et al.*, 1998; Bartels *et al.*, 2004). The relaxation is a special form of homogenisation, which results in material models that predict phase volume fractions at each material point. One may relax w(E) as well by adding a capillarity, since the convexity of the strain energy is determined by the dependence on the highest strain gradient (Sidi Ammi and Torres, 2008),  $w_c(E, \nabla E) = w(E) + c(\nabla E)$ , where  $c(\nabla E)$  must be convex in the strain gradient  $\nabla E$ . This corresponds to an energetic penalisation of sharp strain gradients, as encountered near interfaces. Note that non-quasiconvex minimization problems may arise also in standard material models, see e.g. Carstensen *et al.* (2002).

The second line of work is to introduce a nucleation criterion and a kinetic relation for the phase growth, summarised in Abeyaratne and Knowles (2006). By this, the modelling approach is shifted from energy minimisation to evolution tracking. This may be achieved by any kinetic relation, which must not necessarily be connected to the phase growth. E.g., by incorporating inertia forces, one has to track the propagation of waves. Depending on the kinetic relation, the treatment becomes complicated as well. By introducing a kinetic relation, strain path independence of a purely elastic modelling is resolved. In any case, the resulting model allows to assign definitely a single phase to each material point, i.e. one can speak of a microscale-model. Therefore, in order to obtain macroscale material laws, still a homogenization is required. Moreover, either implicitly or directly, phase boundaries enter the model. These may be regularized (phase field model, Wang *et al.* (2004)) or discrete (sharp interface model, see Hou *et al.* (1999) for a concise outline). Summaries on material modelling approaches which include phase mixtures are given by Ortiz and Repetto (1999), Roubíček (2004) and Zimmer (2006).

In particular, as a regularising kinetic relation, the viscous regularisation enjoys some popularity. It is often applied to single out solutions when damage, strain softening, strain rate softening or phase changes occur (Chaboche *et al.*, 2001; Dias da Silva, 2004; Böhlke *et al.*, 2009; Glüge *et al.*, 2010). It is as well used to overcome the Taylor problem in

crystal plasticity (Hutchinson, 1976), and to transform the algebraic differential equations governing ideal plastic material behaviour to ordinary differential equations (Simo and Hughes, 1998). It is moreover simple to implement, and compliant with thermodynamic considerations.

The material model that is employed here (see Section 4) is derived in detail in Glüge *et al.* (2010). In the same article, the predictions of the model on the microscale have been investigated and compared to experiments. For a comparison with macroscale material behaviour, some kind of homogenisation is required. Therefore, the material model has been combined with the numerical homogenisation via the representative volume element method. Commonly conducted compression tests have been simulated, and the findings are compared to experimental results. In particular, we compare the evolution of the twin volume fraction, of the crystallographic texture, and of the stress state to experimental results obtained for pure magnesium and the magnesium-based alloy AM30. Moreover, the model allows for an observation of the twin propagation in the polycrystal.

# 1.1. Notation

Throughout the work a direct tensor notation is preferred. If an expression cannot be represented in the direct notation without introducing new conventions, its components are given with respect to orthonormal base vectors  $e_i$ , using the summation convention. Vectors are symbolised by lowercase bold letters  $v = v_i e_i$ , second order tensors by uppercase bold letters  $T = T_{ij} e_i \otimes e_j$  or bold greek letters. The second order identity tensor is denoted by I. Fourth-order tensors are symbolised like  $\mathbb{C}$ . The dyadic product is defined as  $(a \otimes b) \cdot c = (b \cdot c)a$ . Matrices are denoted like [A]. A dot represents a scalar contraction. If more than one scalar contraction is carried out, the number of dots corresponds to the number of vectors that are contracted, thus  $a \otimes b \otimes c \cdots d \otimes e = (b \cdot d)(c \cdot e)a$ ,  $\alpha = A \cdots B$  and  $\sigma = \mathbb{C} \cdots \varepsilon$ . When only one scalar contraction is carried out, the scalar dot is frequently omitted, e.g., v = Fw, A = BC. The Rayleigh-product is defined by applying a second order tensor to all base vectors of a tensor. E.g., in case of a fourth order tensor,  $P * \mathbb{C} = C_{ijkl}Pe_i \otimes Pe_j \otimes Pe_k \otimes Pe_l$ , with  $\mathbb{C} = C_{ijkl}e_i \otimes e_j \otimes e_k \otimes e_l$ . Orthogonal tensors are denoted by  $Q_{\beta v} = \tilde{e}_i \otimes e_i$ , mapping one orthonormal basis  $e_i$  into another one  $\tilde{e}_i$ . If Q can be interpreted as a rotation, the optional indexing contains the amount of rotation  $\beta$  and the normalised axial vector v. Two-fold rotations are rotations of amount  $\pi$ . They are denoted as  $R_v = -I + 2v \otimes v$ , with v being the normalised axial vector. The derivative of a vector valued vector function with respect to its argument is denoted like  $v'(w) = \partial v(w)/\partial w = \partial v_i/\partial w_j$   $e_i \otimes e_j$ .

### 1.2. The hexagonal lattice

For a hexagonal lattice, it is convenient to use the Miller-Bravais basis

$$\boldsymbol{a}_1 = a\boldsymbol{e}_1, \tag{1}$$

$$\boldsymbol{a}_2 = a \left( -\frac{1}{2} \boldsymbol{e}_1 + \frac{\sqrt{3}}{2} \boldsymbol{e}_2 \right), \tag{2}$$

$$\boldsymbol{a}_3 = a \left( -\frac{1}{2} \boldsymbol{e}_1 - \frac{\sqrt{3}}{2} \boldsymbol{e}_2 \right), \tag{3}$$

$$\boldsymbol{c} = c\boldsymbol{e}_3,\tag{4}$$

see Figure 2 (Neumann, 1966; Pitteri and Zanzotto, 2002). The lattice parameters c and a represent the height of the cell and the edge length of the base hexagon, respectively, and correspond to the norms of c and a,  $c = \sqrt{c \cdot c}$  and  $a = \sqrt{a \cdot a}$ . Although one usually does not appreciate the use of linearly dependent base vectors, this basis has the advantage that it reflects the hexagonal symmetry. Permutations of the components  $a_{1...3}$ , a change of sign of the c-component or a simultaneous change of sign of all  $a_{1...3}$  yield crystallographically equivalent directions, which are denoted as  $\langle a_1 a_2 a_3 c \rangle$ . Usually, negative components are denoted by  $\bar{x}$  instead of -x. Further, due to the linear dependence of  $a_{1...3}$ , the condition  $a_1 + a_2 + a_3 = 0$  is imposed, and therefore sometimes the third component  $a_3$  is omitted.

To indicate planes, it is advantageous to introduce another basis. This is done by taking the dual basis  $(\tilde{a}_1, \tilde{a}_2, \tilde{c})$  of

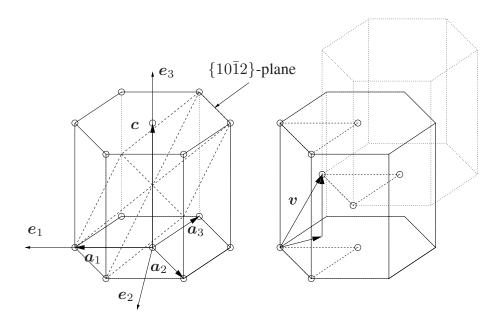


Figure 2: Simple hexagonal lattice with Miller-Bravais basis (left), hexagonal close packed multilattice constructed from the simple lattice by introducing additional translations in  $\boldsymbol{v} = \langle \frac{1}{3} 0 \frac{1}{3} \frac{1}{2} \rangle$  (right).

 $(a_1, a_2, c)$  and defining the base vectors

$$a_1^* = \frac{2}{3}\tilde{a}_1 - \frac{1}{3}\tilde{a}_2 = \frac{2}{3a^2}a_1,\tag{5}$$

$$a_2^* = -\frac{1}{3}\tilde{a}_1 + \frac{2}{3}\tilde{a}_2 = \frac{2}{3a^2}a_2,\tag{6}$$

$$a_3^* = -\frac{1}{3}\tilde{a}_1 - \frac{1}{3}\tilde{a}_2 = \frac{2}{3a^2}a_3,\tag{7}$$

$$\boldsymbol{c}^* = \tilde{\boldsymbol{c}} = \frac{1}{c^2} \boldsymbol{c}.$$
(8)

This basis again satisfies  $a_1^* + a_2^* + a_3^* = 0$ , but it is not the dual basis of  $(a_1, a_2, a_3, c)$ . It also has the advantage that crystallographically equivalent planes are connected by permutations of the components and changes of sign as stated above. Again, the components should be restricted to  $a_1^* + a_2^* + a_3^* = 0$ . If this is done, several practical simplifications are obtained: If a normal vector is given with respect to the basis  $(a_1^*, a_2^*, a_3^*, c^*)$ , the reciprocals of its components correspond to the piercing point distances of the plane with the base vectors  $(a_1, a_2, a_3, c)$ . Therefore, the plane  $\{10\overline{1}2\}$  can be visualised by considering the points  $a_1, -a_3$  and 1/2c (see Figure 2). Moreover, one can easily see whether direction and normal vectors are perpendicular to each other by calculating the scalar product as if  $(a_1, a_2, a_3, c)$  and  $(a_1^*, a_2^*, a_3^*, c^*)$  were dual bases. One notes easily that  $\langle 10\overline{1}1 \rangle$  and  $\{\overline{1}012\}$  are perpendicular to each other:

$$a_{1} - a_{3} + c) \cdot (-a_{1}^{*} + a_{3}^{*} + 2c^{*}) = a_{1} \cdot (a_{3}^{*} - a_{1}^{*}) - a_{3} \cdot (a_{3}^{*} - a_{1}^{*}) + 2c \cdot c^{*}$$
  
= -1 - 1 + 2 = 0. (9)

### 2. Uniaxial testing of extruded magnesium

Twinning in magnesium has been studied in detail firstly by Reed-Hill and Robertson (1957a,b); Partridge (1965); Roberts and Partridge (1966); Wonsiewicz and Backofen (1967); Kelley and Hosford (1968). Since these pioneering works, a large amount of literature concerning twinning in magnesium and its alloys has been published. In hexagonal metals, the

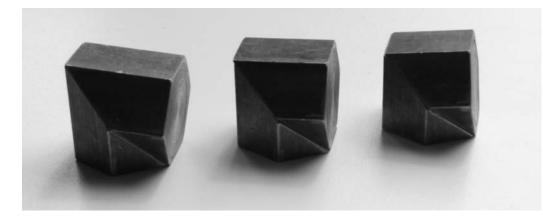


Figure 3: The c/a ratio controls the direction and the magnitude of the shear deformation accompanying  $\{10\overline{1}2\}$  twinning. Left:  $c/a > \sqrt{3}$ , twinning shear increases width of the structure, leading to *c*-axis compression. Centre:  $c/a = \sqrt{3}$ , width and height do not change (the mean deformation is zero, no  $\{10\overline{1}2\}$  twinning). Right:  $c/a < \sqrt{3}$ , twinning shear increases the height of the structure, leading to *c*-axis elongation.

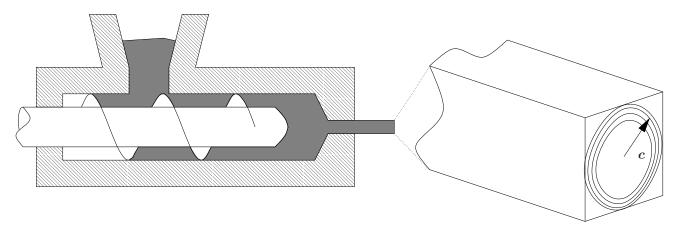


Figure 4: Cross section of an extruder. The material enters through the upper inlet funnel, and is pressed through the outlet on the right. The resulting rod is strongly textured.

twins are usually categorised as extension or compression twins, depending on whether they appear under elongation or compression along the *c*-axis. Magnesium has  $c \approx 0.52103$ nm and  $a \approx 0.32094$ nm, which gives  $c/a \approx 1.62345$ , i.e. it is quite close to the densest possible packing with  $c/a = \sqrt{8/3}$ . The unit cell is slightly less high than thick. This causes the  $\{\overline{1}012\}\langle\overline{1}011\rangle$  twins to be extension twins (see Figure 3), while twinning along the  $\{10\overline{1}1\}, \{10\overline{1}3\}, \{30\overline{3}4\}$  and  $\{10\overline{1}5\}$  planes (Meng *et al.*, 2008) occurs under *c*-axis compression. Recently, Stanford (2008) observed  $\{11\overline{2}1\}$ -twinning in the magnesium alloy WE54.

In a recent work Al-Samman and Gottstein (2008), plane strain compression tests are carried out on cuboid-shaped AZ31 samples with different processing histories. One of them is an extruded sample, that is compressed along the extrusion direction (Figure 4). Extruded magnesium is textured such that the *c*-axes are aligned approximately uniformly and perpendicular around the extrusion direction, i.e. a compression along the extrusion direction results in a *c*-axis elongation and vice versa. In a compression test, the strongly textured material undergoes a complete shift of texture, see Figure 5.

However, the impressive change of texture does not occur when the loading direction is reversed. Moreover, one observes a pronounced strength differential effect. The cause for this is the uni-directionality of twinning. The *c*-axis elongation is accommodated by  $\{\bar{1}012\}$  twins, while compression twins (mostly  $\{\bar{1}011\}$ ) accommodate *c*-axis compression, i.e. elongation along the extrusion direction. These twinning modes exhibit strong morphological differences. The  $\{\bar{1}012\}$  tension twins are activated very easily, (namely at a shear stress of approximately 2.7MPa in pure magnesium, Koike

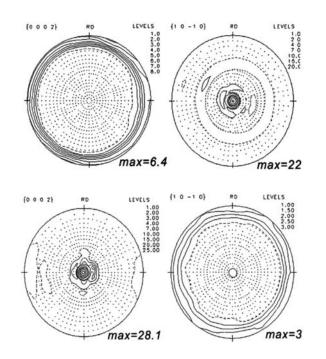


Figure 5: (0002) (left) and ( $10\overline{1}0$ ) (right) pole figures before (above) and after (below) the compression test at a nominal strain of  $\varepsilon = 0.28$  (courtesy of Al-Samman and Gottstein (2008)). The projection direction is parallel to the extrusion direction. As { $10\overline{1}2$ } twinning reorients the *c*-axis about approximately  $86^{\circ}$ , the outer ring (upper left figure) transforms into the centre peek (lower left figure). The slight deviation from the approximately rotational symmetric starting texture comes from the asymmetry of the loading (plane strain compression, two opposing faces are kept fixed).

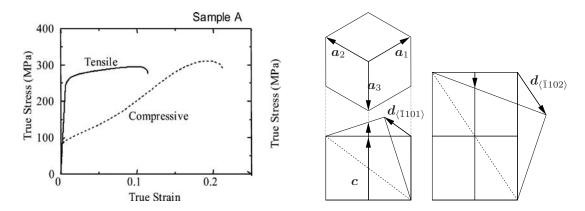


Figure 6: Strength differential effect in the AZ31 magnesium alloy (left, courtesy of Chino *et al.* (2008)), sketch of  $\langle \bar{1}101 \rangle \{1\bar{1}02\}$  extension and  $\langle \bar{1}102 \rangle \{1\bar{1}01\}$  compression twinning (right). Due to the approximately perpendicular alignment of the *c*-axis with respect to the extrusion direction, the extension twins (twins that form under *c*-axis elongation) develop in compression test along the extrusion direction, while compression twins (twins that form under *c*-axis compression) show in elongation tests parallel to the extrusion direction.

(2005)), and their boundaries are mobile. The  $\{\overline{1}011\}$  compression twins are thin, pinned lamellas. Instead of growing in thickness like the elongation twins, double twinning (first  $\{10\overline{1}1\}$  compression followed by  $\{10\overline{1}2\}$  extension twins) is observed as loading continues (Yi *et al.*, 2009).

Therefore, in a compression test, the major deformation mechanism are the  $\{\overline{1}012\}$  elongation twins. After virtually occupying the entire volume, elongation twinning is no more disposable. Due to the reorientation of the *c*-axis of approximately 86°, the deformation is then accommodated by  $\{\overline{1}011\}$  compression twinning (Wonsiewicz and Backofen, 1967; Kelley and Hosford, 1968), as it occurs from the beginning if the contrary loading direction is chosen. As depicted in Figure 6, the stress level is then approximately the same as in the tension test. Due to the immobile interfaces of the compression twins, the deformation accommodated before fracture is much lesser than in case of elongation twinning. The double twins have been identified to be crack initiation sites (Hartt and Reed-Hill, 1968; Yin *et al.*, 2008).

# 3. Characteristics of $\{\overline{1}012\}$ and $\{\overline{1}011\}$ twinning

Summarising the foregoing section roughly,  $\{\overline{1}012\}$  tension twins allow for large deformation accommodation, while  $\{\overline{1}011\}$  compression twins precede fracture. A similar behaviour is observed in titanium (Serra and Bacon, 1996; Ungár *et al.*, 2008) and zinc (Lay and Nouet, 1994), which suggests that the morphological difference between the twinning modes is intrinsic to the hexagonal lattice structure. It is explained by the characteristics of the distinct interfaces and partial dislocations belonging to each twinning mode.

A first explanation is given in a series of articles by Serra and Bacon (Bacon and Liang, 1986; Serra and Bacon, 1986, 1991, 1996), who analysed twinning with the molecular dynamics technique. Firstly, they examined which of the different many-body potentials given in the literature suite best to each hcp metal (Bacon and Liang, 1986). Igarashi *et al.* (1991) adopted parameters of the many-body potentials such that they reproduce the elastic properties and c/a ratio for eight hcp metals. With the potentials at hand, the stacking fault and interface energies have been calculated, and found to be in agreement with experiments (Serra and Bacon, 1986). In Serra and Bacon (1991), the mobility of partial dislocations belonging to different twin interfaces has been studied by means of molecular dynamics. It is found that dislocations in  $\{10\overline{1}2\}$  and  $\{11\overline{2}1\}$  boundaries are very glissile, but sessile in  $\{10\overline{1}1\}$  and  $\{11\overline{2}2\}$  interfaces. In Serra and Bacon (1996), the interaction between basal slip dislocations and different twin interfaces has been studied. It is found that if a basal slip dislocation hits a  $\{10\overline{1}2\}$  interface, a source for  $\{10\overline{1}2\}$  partial dislocations is created, which forms pairs of partial dislocations if a shear strain of approximately  $\pm 0.005$  is applied. The source therefore provides a mechanism to move the interface gradually by generating a pair of partial dislocations, as long as the load is not removed and no obstacle is met. The converse is reported for a basal slip dislocation that hits a  $\{10\overline{1}1\}$  interface. It creates there a pair of partial dislocations, but not an independent source for twinning dislocations. Together with the findings from Serra and Bacon (1991), a convincing explanation for  $\{10\overline{1}2\}$ -twinning being the most prominent twinning mode in hcp metals is obtained.

Another explanation for the needle-like  $\{10\overline{1}1\}$  twinning and the extensive  $\{10\overline{1}2\}$  twinning is that the  $\{10\overline{1}1\}$  twins produce a larger shear strain. Therefore, to accommodate a certain deformation, compared to  $\{10\overline{1}2\}$  twinning, less volume fraction of  $\{10\overline{1}1\}$  twins is necessary (Bingert *et al.*, 2002; Jiang *et al.*, 2007). At least for magnesium this explanation is rather improbable, as the corresponding shear numbers  $\gamma_{\{10\overline{1}2\}} \approx 0.13$  and  $\gamma_{\{10\overline{1}1\}} \approx 0.137$  differ only slightly.

A third explanation is given by the recent works of Li (Li and Ma, 2009b,a). Summarising their findings, the morphological difference between  $\{10\overline{1}1\}$  and  $\{10\overline{1}2\}$  twinning arise from different propagation mechanisms. In case of the  $\{10\overline{1}1\}$  twinning, the interface movement rests upon the movement of partial dislocations, while in case of the  $\{10\overline{1}2\}$  twinning, atomic shuffling appears to play the leading role, and no pronounced partial dislocation is observed. Therefore, unlike  $\{10\overline{1}2\}$  twinning, the  $\{10\overline{1}1\}$  twin propagation is restricted by the partial dislocation density, which renders the  $\{10\overline{1}2\}$  interfaces more glissile compared to the  $\{10\overline{1}1\}$  interfaces. Interestingly, these findings are not entirely in agreement with the results of Serra and Bacon.

Since the  $\{1012\}$  twinning mode allows for large strains, it is the adequate candidate to be tested with a continuum theory. Therefore, it is implemented in the material model that is presented in the next section, and compression tests on extruded magnesium are carried out with help of the RVE method.

# 4. The material model

The material model is based on a nonconvex elastic energy plus the viscous regularisation, in terms of the second Piola-Kirchhoff-Stresses

$$T = \frac{1}{2} \left( \frac{\partial \tilde{w}}{\partial C} + \eta C^{-1} \dot{C} C^{-1} \right), \tag{10}$$

where the elastic energy  $\tilde{w}$  is a stress potential with respect to the right Cauchy-Green tensor C. The viscosity discussed in the introduction is denoted by  $\eta$ . The elastic energy is obtained by combining the elastic energies of the possible configurations in a regularised version of the Ball and James-approach (Ball and James, 1987)

$$\tilde{w}(\boldsymbol{C}) = \min(w_1(\boldsymbol{C}), w_2(\boldsymbol{C})...w_n(\boldsymbol{C})).$$
(11)

The individual strain energies are obtained by exploiting the isomorphy of the parent and the twin lattices (Bertram, 2003), embodied by the plastic transformations  $P_i$ . To avoid an overestimation of the critical twinning stress, a modification of the individual strain energies is necessary, which is done with the help of the indicator functions  $\phi_i$ . Inside the parent configuration, basal slip is possible, which is approximated by the card glide mechanism. The index 0 indicates the parent configuration, while the indices 1...6 run over the possible twin variants, and sums are explicitly written. Firstly, eq. (11) is replaced by the regularization

$$\tilde{w} = \sum_{i=0}^{n} a_i w_i \qquad a_i = \frac{g_i}{\sum_{j=0}^{6} g_j} \qquad g_i = \frac{h(w_i)}{1 - h(w_i)} \qquad h_i = \exp(-kw_i), \tag{12}$$

where the regularization parameter k is introduced. Taking the limit  $k \to \infty$ , eq. (12) approaches eq. (11) from above. The individual strain energies are given by

$$w_i = \frac{1}{2} \boldsymbol{E}_i \cdots \boldsymbol{\mathbb{C}} \cdots \boldsymbol{E}_i \qquad \text{if } \phi_i(\boldsymbol{E}_i) \le 0 \qquad (13)$$

$$w_i = \boldsymbol{E}_i \cdot \cdot \mathbb{C} \cdot \cdot \boldsymbol{E}_{i,\text{crit}} - \frac{1}{2} \boldsymbol{E}_{i,\text{crit}} \cdot \cdot \mathbb{C}_0 \cdot \cdot \boldsymbol{E}_{i,\text{crit}} \qquad \text{if } \phi_i(\boldsymbol{E}_i) > 0 \tag{14}$$

The indicator functions are given by

$$\phi_0(\boldsymbol{E}_0) = \sum_{i=1}^6 \langle \gamma_i / \gamma_{\text{twin}} \rangle^m - 1 \qquad \qquad \gamma_i = 2\boldsymbol{E}_0 \cdot \boldsymbol{M}_i \tag{15}$$

$$\phi_i(\boldsymbol{E}_i) = \frac{\gamma_i}{\gamma_{\text{twin}}} - 1 \qquad \gamma_i = 2\boldsymbol{E}_i \cdot \boldsymbol{M}_i \qquad i = 1...6, \tag{16}$$

with the critical twinning shear  $\gamma_{\text{twin}}$  and the Schmid tensors  $M_i = d_i \otimes n_i$ . The straining with respect to the stress-free configurations of each phase is

$$\boldsymbol{E}_{i}(\boldsymbol{C}) = \frac{1}{2} (\boldsymbol{P}_{i}^{T} \boldsymbol{C} \boldsymbol{P}_{i} - \boldsymbol{I}).$$
(17)

The plastic transformations  $P_i$  contain the twinning shear  $S_i$  and the lattice reorientation  $R_{n_i}$ ,

$$P_i = P_0 P_{0i} \qquad i = 1...6, \tag{18}$$

$$\boldsymbol{P}_{0i} = \boldsymbol{S}_i^{-1} \boldsymbol{R}_{\boldsymbol{n}_i},\tag{19}$$

$$\boldsymbol{S}_i = \gamma_0 \boldsymbol{d}_i \otimes \boldsymbol{n}_i \tag{20}$$

$$\boldsymbol{R}_{\boldsymbol{n}_i} = -\boldsymbol{I} + 2\boldsymbol{n}_i \otimes \boldsymbol{n}_i. \tag{21}$$

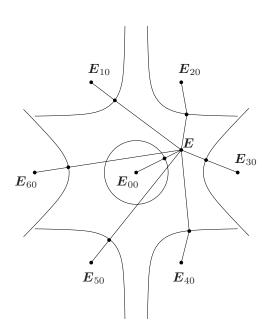


Figure 7: Let the sheet represent all possible strain states. The stress-free states are denoted by  $E_{i0}$ , and the curved lines are the isolines  $\phi_i(E) = 0$ . The piercing points represent the strains  $E_{i,crit}$ . The  $E_i$  correspond to E from the viewpoint of each stress-free configuration  $E_{i0}$ .

 $P_0$  relates the elastic reference law to the reference placement, which is in the parent configuration. The  $E_{i,crit}$  are, together with  $\lambda$ , defined implicitly by the orthogonal projection

$$\phi_i(\boldsymbol{E}_{i,\mathrm{crit}}) = 0, \qquad \boldsymbol{E}_i = \boldsymbol{E}_{i,\mathrm{crit}} + \lambda \frac{\partial \phi_i}{\partial \boldsymbol{E}} \Big|_{\boldsymbol{E}_{i,\mathrm{crit}}}$$
(22)

At least the  $E_i$  and  $E_{i,crit}$  can be schematically visualised, see Figure 7. This is, so far, the elastic energy. Since we replaced the algebraic condition (11) by a differentiable function, the elastic energy  $\tilde{w}$  may enter in eq. (10).

In order to account for basal slip, the collective of basal slip systems is approximated by the card glide mechanism.  $n_b$  corresponds to the base plane normal, while the slip direction  $d_b$  is obtained by projecting the stress vector into the base plane. The plastic transformation of the parent evolves corresponding to

$$-\boldsymbol{P}_{0}^{-1}\dot{\boldsymbol{P}}_{0} = \dot{\gamma}\boldsymbol{d}_{b}^{*} \otimes \boldsymbol{n}_{b}, \qquad \boldsymbol{d}_{b}^{*} = \frac{\boldsymbol{d}_{b}}{\|\boldsymbol{d}_{b}\|},$$
(23)

with

$$\boldsymbol{d} = ((\boldsymbol{I} - \boldsymbol{n}_b \otimes \boldsymbol{n}_b) \tilde{\boldsymbol{F}}^{-1} \boldsymbol{\sigma} \tilde{\boldsymbol{F}}^{-T}) \cdot \boldsymbol{n}_b, \qquad \tilde{\boldsymbol{F}} = \boldsymbol{F} \boldsymbol{P}_0.$$
<sup>(24)</sup>

 $\dot{\gamma}$  is determined consistently with the elastic law. I.e., during the plastic flow, the resolved shear stress in the card glide system is equal to the flow stress,

$$\tau_{\text{basal}} = \boldsymbol{\sigma} \cdot \boldsymbol{d}_b^* \otimes \boldsymbol{n}_b. \tag{25}$$

The material parameters are given with respect to the elastic reference law.  $e_1$  is parallel to  $a_1$  while  $e_3$  is parallel to the *c*-axis. The elastic stiffness tetrad of single crystalline magnesium (Simmons and Wang, 1971), with respect to the basis  $B_1 = e_1 \otimes e_1$ ,  $B_2 = e_2 \otimes e_2$ ,  $B_3 = e_3 \otimes e_3$ ,  $B_4 = \sqrt{2}/2(e_1 \otimes e_2 + e_2 \otimes e_1)$ ,  $B_5 = \sqrt{2}/2(e_1 \otimes e_3 + e_3 \otimes e_1)$ ,

 $B_{6} = \sqrt{2}/2(e_{2} \otimes e_{3} + e_{3} \otimes e_{2}), \text{ is}$   $\mathbb{C} = \begin{bmatrix} 56.49 & 23.16 & 18.10 & 0 & 0 & 0 \\ 56.49 & 18.10 & 0 & 0 & 0 \\ & 58.73 & 0 & 0 & 0 \\ & & 2 \times 16.81 & 0 & 0 \\ & & & & 2 \times 16.81 & 0 \\ & & & & 56.49 - 23.16 \end{bmatrix} B_{i} \otimes B_{j}, \quad (26)$ 

in GPa.  $B_i$  is an orthonormal vector basis for symmetric 2nd order tensors, i.e. a fourth order tensor with both subsymmetries can be denoted as a second order tensor with respect to  $B_i$ . The six structural tensors belonging to the  $\{10\overline{1}2\}\langle\overline{1}011\rangle$  twin systems are given by

$$\boldsymbol{M}_1 = \boldsymbol{d}_1 \otimes \boldsymbol{n}_1 \tag{27}$$

$$\boldsymbol{d}_1 = \cos(\alpha)\boldsymbol{e}_2 + \sin(\alpha)\boldsymbol{e}_3 \tag{28}$$

$$\boldsymbol{n}_1 = -\sin(\alpha)\boldsymbol{e}_2 + \cos(\alpha)\boldsymbol{e}_3 \tag{29}$$

$$M_i = Q_{\pi/3}^{i-1} * M_1, \qquad i = 2...6$$
(30)

i.e. by rotating the twin system  $M_1$  in the sixfold symmetric hexagonal cell, with

$$\alpha = \operatorname{atan}(c/(a\sqrt{3})). \tag{31}$$

For magnesium and its alloys,  $c/a \approx 1.623$ . The twinning shear for the  $\{10\overline{1}2\}\langle\overline{1}011\rangle$  twin systems is given by

$$\gamma_0 = \frac{\sqrt{3}}{c/a} - \frac{c/a}{\sqrt{3}},\tag{32}$$

i.e.  $\gamma_0 \approx 0.13$  (Christian and Mahajan, 1995).

The critical shear strain is taken as  $\gamma_{twin} = 0.006\gamma_0$ , which allows to estimate the critical shear stress (CSS) for twinning by  $\tau_{crit} = G\gamma_{twin} \approx 0.006 \times 0.13 \times 17000$  MPa $\approx 13$  MPa. For  $\{10\overline{1}2\}\langle\overline{1}011\rangle$  twinning in Mg, one can find values ranging from 2.7 to 2.8 MPa (Koike, 2005) to 14 to 19 MPa (Zhou *et al.*, 2008) and 40 to 50 MPa for a Mg alloy (Wang and Huang, 2007). The actual value depends strongly on the twin criterion that is employed by the experimenters. Since no analytical estimation of the macroscale material law can be given, we determined the value of 13 MPa inversely by adopting  $\gamma_{twin} = 0.006\gamma_0$  to the experiments, see Section 5.4. The corresponding CSS falls well into the range of reasonable values.

The parameter k should be chosen such that the linear elastic behaviour near the stress-free configuration is reproduced sufficiently well, which is the case as k tends to  $\infty$ . On the other hand, a very large k results in an approximation of the algebraic condition (11), i.e. a very sharp transition. Since  $\gamma_{twin}$  limits the linear elastic range, k should not be determined independently on  $\gamma_{twin}$ . We found k = 0.25 to be a reasonable compromise between a smooth transition and a good approximation of the individual elastic laws of each phase.

For the viscosity, the value  $\eta = 10000$  MPa s has been estimated. Again, a compromise between a preferably small viscous contribution to the stresses and stable time integration with reasonable large time steps has to be found. Its choice is strongly connected to the simulation setup, in particular to the mean deformation rate. For the RVE-simulations discussed in the next section, a variation of  $\eta$  did not show an essential effect on the apparent stress strain relation, i.e. it is considered to be sufficiently small. The average viscous contribution can be estimated by multiplying  $\eta$  with the average strain rate (0.2E-3), resulting in 2MPa, which is relatively small compared to the average stresses found in the homogenisation procedure. The regularisation parameter of the phenomenological model adaption of the strain energy is taken to be m = 10, which results in a fairly sharp approximation of the non-differentiable single crystal yield surface  $\tau_{\rm crit} = \max(\tau_1, \tau_2 \dots \tau_6)$ .

For the basal glide, only the critical shear stress  $\tau_{\text{basal}}$  enters the card glide. It is observed that the critical  $\{10\overline{1}2\}\langle\overline{1}011\rangle$  twinning stress and the basal slip shear stress are related by  $\tau_{\text{crit}}/\tau_{\text{basal}} \approx 2...4$ . Therefore,  $\tau_{\text{basal}}$  is set to 4 MPa, and strain hardening is neglected.

Table 1: Material parameters of the present model.		
parameter	value	source
$\mathbb{C}$	see eq. (26)	measurement, Simmons and Wang (1971)
$\gamma_0$	0.13	geometrical considerations (eq. 20)
$\gamma_{\mathrm{twin}}$	$0.006\gamma_0$	estimation such that $\tau_{\rm crit} \approx 13$ MPa, Zhou <i>et al.</i> (2008)
k	0.25	estimation
$\eta$	10000 MPa s	estimation
m	10	estimation
$ au_{\mathrm{basal}}$	4 MPa	estimation such that $\tau_{\rm crit}/\tau_{\rm basal} \approx 3$ , Li <i>et al.</i> (2007)

### 5. Simple compression of an RVE

In order to obtain results that are comparable to experimental data, the RVE method is used to simulate the simple compression of an extruded magnesium alloy along the extrusion direction. The crystallographic texture of the latter is such that the *c*-axes are aligned approximately perpendicular to the extrusion direction, i.e., the compression along the extrusion direction results in c-axis elongation, which is accommodated by  $\{10\overline{1}2\}\langle\overline{1}011\rangle$  twinning (see Jiang et al. (2007); Al-Samman and Gottstein (2008)).

#### 5.1. Model setup

The FE model of the RVE consist of a regularly meshed cube with  $40 \times 40 \times 40$  fully integrated linear hexahedron elements (C3D8 in the ABAQUS element library). The initial microstructure has been approximated by a periodic Voronoi tessellation, consisting of 20 grains, Figure 8. The limited number of grains is necessary to provide a reasonable discretization of each grain, though the grains are partitioned by twinning. The phases are assigned integration-point-wise, i.e. the model contains multiphase elements. The crystal orientations are restricted such that the c-axes do not deviate more than  $15^{\circ}$  from the plane of compression, and are uniformly distributed. This value has been estimated from the texture sharpness given by Jiang et al. (2007). No preferred orientation of the remaining degree of freedom (rotating the  $a_i$  around the c-axis) has been established. The displacement boundary conditions are periodic on the entire surface of the cube, while the tractions are anti-periodic. The 11-component of the mean displacement gradient with respect to the orthonormal base system used for the model description have been constrained,

$$\boldsymbol{H} = \begin{bmatrix} f(t) & 0 & 0\\ 0 & \cdot & 0\\ 0 & 0 & \cdot \end{bmatrix} \boldsymbol{e}_i \otimes \boldsymbol{e}_j, \tag{33}$$

while  $H_{22}$  and  $H_{33}$  have not been constrained. Instead, the mean reaction forces along the  $e_2$  and  $e_3$  directions have been constrained at the corresponding faces to be equal to zero, in order to obtain the average uniaxial stress state along the  $e_1$ direction.

### 5.2. Numerical homogenization

The apparent material behaviour is obtained by relating average dynamic and kinematic quantities to the RVE. The kinematic and dynamic coupling has been carried out in F and the first Piola-Kirchhoff stresses S by integrals in the reference placement,

$$\bar{\boldsymbol{F}} = \int_{\Omega_0} \boldsymbol{F} \mathrm{d} V_0 \tag{34}$$

$$\bar{\boldsymbol{S}} = \int_{\Omega_0} \boldsymbol{S} \mathrm{d} V_0. \tag{35}$$

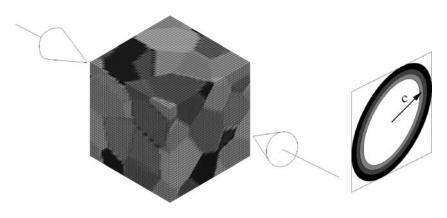


Figure 8: FE Model of the RVE, with schematic pole figure of the c-axes. The greyscale exemplifies the periodic Voronoi structure of the grains.

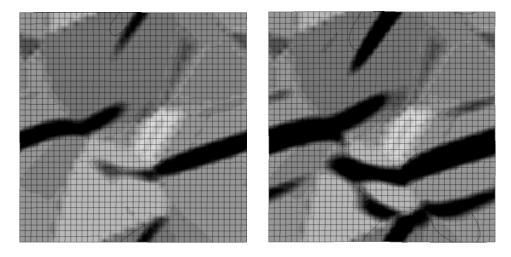


Figure 9: Cut through the RVE, where the cutting plane normal corresponds to the compression direction. The grey-scaling represents the grain structure. One can see the propagation of a twin (black) over a grain boundary. The left frame is taken shortly before the right frame.

However, only  $\bar{S}$  needs to be extracted from the RVE, since  $\bar{F}$  is prescribed. From  $\bar{F}$  and  $\bar{S}$ , the Cauchy stresses

$$\bar{\boldsymbol{\sigma}} = \frac{1}{\det \bar{\boldsymbol{F}}} \bar{\boldsymbol{S}} \bar{\boldsymbol{F}}^T \tag{36}$$

and the logarithmic strains are determined. Due to the diagonal form of  $\bar{F}$ , the logarithmic straining in the  $e_1$  direction is obtained by  $\varepsilon_{\log} = \ln \bar{F}_{11}$ . For more details on the RVE method the reader is referred to the works of Suquet (1987); Nemat-Nasser (1999); Markov and Preziosi (2000); Zohdi and Wriggers (2001); Miehe (2003).

### 5.3. General observations

Initially, the stress-strain relation is linear elastic, as expected. Due to the weak anisotropy of magnesium, the deformation and the stresses are relatively homogeneous at this stage. At approximately 2% of logarithmic strain, twins nucleate and spread rapidly over the FE model. In Figure 9, the propagation of a twin over a grain boundary is illustrated. In Figure 10, a sequence of states illustrating the twin spreading in the RVE is given. The incorporation of basal glide does not significantly alter the results, which is due to the approximately perpendicular alignment of the basal planes to the principal stress direction. The microscale features of the material model are studied in detail in Glüge *et al.* (2010). Here, the focus is on the macroscale predictions.

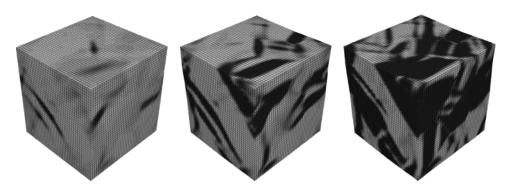


Figure 10: Twin spreading on the RVE, at a nominal compression strain of 2.5%, 2.9% and 4.6%, from left to right. The compression direction is normal to the lower right face of each cube.

### 5.4. Comparison to experimental findings

As a reference, the works of Reed-Hill (1973) and Jiang *et al.* (2007) have been used, where compression tests for two magnesium alloys (AM30 and AZ31, Jiang *et al.* (2007)) and pure magnesium (Reed-Hill, 1973) are documented. The material model and simulation setup correspond to pure magnesium without precipitates. However, due to the lack of data for pure magnesium, the twin volume fraction and texture evolution are compared to experimental findings obtained for the magnesium alloy AM30.

Stress-strain relation. Comparing to the compression stress-strain response given by Jiang *et al.* (2007) (Figure 17), one finds that the experimental results display a considerable strain hardening, while in the simulations a pronounced zero-hardening plateau is found. This is due the fact that the hardening behaviour of AM30 is very complex due to precipitates, which is not captured by the model. This explanation is furnished by the fact that the stress strain response is in considerable agreement with the compression experiments with pure magnesium (Reed-Hill, 1973), which displays a less complicated hardening behaviour due to the lack of particles and precipitates, see Figure 12. It is found that the zero-hardening-plateau at approximately 60 MPa ( $\approx 8.7$  ksi) corresponds to the twin nucleation phase. At approximately 3% of logarithmic strain, the nominal stress increases constantly, which coincides with the point where volume-filling twinning starts seriously. Similar findings are given by Muránsky *et al.* (2009). The hardening is explained by the fact that the twins form firstly at stress concentration points, or expressed differently, at the most favourable twinning sites. For further twinning, the loading must be increased in order to activate the less favoured twinning sites. One notes that the hardening rate is overpredicted in the simulations. This is due to the fact that the material model does not capture secondary twinning and slipping inside the twins, which renders them stiffer as in reality.

*Twin volume fraction evolution.* In Figure 11, graphs for the twin volume fraction evolution in the experiments and the simulations are depicted. One notes that the evolution of the twin volume fraction is qualitatively in good agreement with the experimental findings. The rapidly increasing twinning rate at 3 to 5% of logarithmic strain, as well as the saturation are captured by the model. Therefore, it is to be expected that the crystallographic texture evolution are in good accordance, as twinning dominates the texture evolution for this particular experiment. Quantitatively, the simulated twin volume fraction is overestimated. This discrepancy is discussed in the last paragraph of this section.

*Texture evolution.* The RVE-simulations allow to compare the texture evolution with experimental results. At a material point, the significant orientation is assumed to be given by the phase with the smallest strain energy. Due to the phenomenological model adaption, the strain energy invariance is not exactly met by the model, i.e. a definite orientation can be extracted at each of the  $8 \times 40^3$  integration points of the FE model. The *c*-axes of 20 initial orientations deviate at most by  $15^{\circ}$  from the compression plane, see Figure 13 for pole figures of the initial orientation distribution. The sequence of *c* and *a* pole figures for the compression test is given in Figure 14. One notes that the texture evolution corresponds qualitatively well to experimental results of Jiang *et al.* (2007), although the rate at which the texture shifts is overestimated.

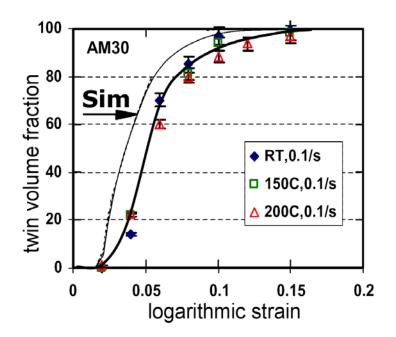


Figure 11: Comparison of the experimental (Jiang et al., 2007) and the RVE-simulated twin volume fraction evolution.

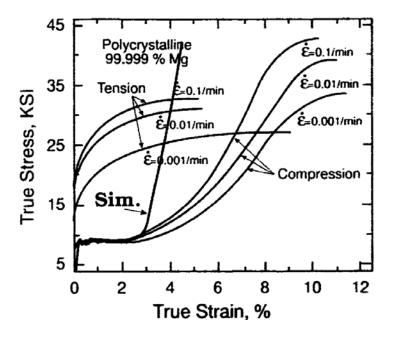


Figure 12: Comparison of the experimental and the RVE-simulated stress evolution (Cauchy stress over logarithmic strain). Courtesy of S.N. Monteiro, experimental data firstly published in Reed-Hill (1973).

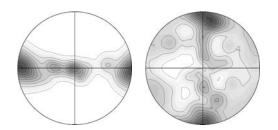
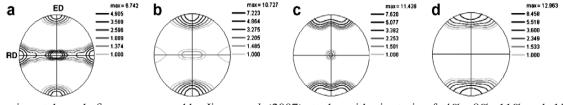


Figure 13: c and a pole figures of the initial orientation distribution, with  $I_{c_{max}} = 9.403$  and  $I_{a_{max}} = 5.173$ . The projection plane is parallel to the compression direction. The pole figures are calculated using a Mises-Fisher (Fisher, 1953) distribution with a half-width of 20° around the individual orientations.



Experimental c pole figures measured by Jiang et al. (2007) at a logarithmic strain of -4%, -8% -11% and -15%.

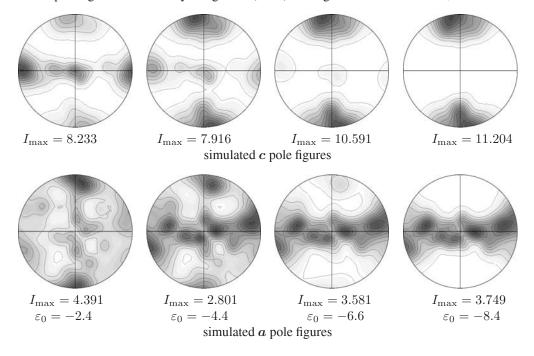


Figure 14: c and a pole figures for the compression test. The projection plane is parallel to the compression direction. The pole figures are calculated using a Mises-Fisher distribution with a half-width of 20° around the individual orientations.

*The role of basal glide*. Not surprising, the basal glide has virtually no effect on the overall material behaviour, which is due to the approximately perpendicular orientation of the basal plane to the compression direction. At the onset of twinning, very weak basal glide is observed. The model does not include basal slip in the twins. Therefore, as the deformation continues and the twin volume fraction increases, the basal slip ceases completely.

*Differences between simulations and experiments.* Since the model captures only first order  $\{10\overline{1}2\}\langle\overline{1}011\rangle$  twins and basal glide in the parent crystal, some deviations from experimental findings should be expected. There are more deformation mechanisms contributing the the material behaviour, namely very few pyramidal glide, secondary twinning, glide inside the twins, other primary twinning modes and damage.

First of all, the twins deform purely elastically, i.e. they behave stiffer as in reality. Therefore, in the case of a twin saturation at a volume fraction of 100%, no stress saturation is obtained. Instead, the stress-strain response approaches the linear elastic material behaviour, which explains the overestimation of the hardening after the zero-hardening plateau.

Secondly, a comparison of the stress strain relation with AM30 is even more risky. As mentioned before, precipitates strengthen the material by acting as stiff inclusions, hindering twinning and slip. This is not included in the model setup, allowing for a more easy twin formation at a lower stress level. Therefore, the twin volume fraction and consequently the texture evolution are overestimated.

### 6. Summary

The model proposed by Glüge *et al.* (2010) is used in a simple compression simulation of an RVE, where the orientation distribution is similar to the one that is experimentally observed in extruded magnesium. It is found that the predicted twin structure displays the main features of experimentally observed twin structures. The twins form as plates inside the grains. Near the grain boundary, the twinning induced misfit strain causes the nucleation of a twin in the neighbouring grain, i.e. the twins are able to propagate across grain boundaries. The average twin volume fraction and the texture evolution correspond well to experimental findings of Jiang *et al.* (2007). Due to the complicated hardening behaviour owed to twin-particle interactions, the hardening behaviour of magnesium alloy is underestimated. In the phase of extensive twinning, the model predicts a zero hardening plateau, which is in accordance to experimental observations on pure magnesium (Reed-Hill, 1973). At the end of the phase of extensive twinning, the stresses are overpredicted in both cases. This is due to the lack of the following deformation mechanisms: secondary twinning, slip inside the twins, and damage. Due to the model setup, the principal direction of straining is approximately perpendicular to the basal slip planes, which renders the role of basal glide as secondary. The slip-twin interaction is studied in Glüge *et al.* (2010).

The presented modelling approach is able to predict the features of deformation twinning on the microscale (Glüge et al., 2010) as well as on the macroscale. However, problems should not be concealed. First of all, to predict the macroscopic material behaviour, the numerical homogenisation via the RVE method needs to be employed. The computational effort is therefore too large for practical forming process simulations. There are as well some fundamental difficulties. The most problematic fact is that twinning is connected to the movement of partial dislocations. This induces a strain path-dependence and energy dissipation. Both are neglected by any pseudoelastic modelling. For example, the elastic modelling allows, in principle, phase changes from one twin variant to another one without passing through the parent phase as the intermediate configuration. Such behaviour is not realistic due to the kinetic process underlying to the twin formation. The conclusion is that the pseudoelastic modelling cannot be applied if severe strain path changes occur. For the same reason, higher order twinning has to be excluded from the model, as the higher order twins are only accessible by a specific series of twinning operations. This strain path dependence can not be reflected by an elastic modelling with a static strain energy. The latter may be resolved by proposing a non-static strain energy density. Moreover, the strain energy invariance of conjugate twins restricts the elastic modelling to crystallographically equivalent conjugate twins. An example for crystallographically distinct conjugate twins are the  $\{01\overline{1}1\}\langle 01\overline{1}2\rangle$  and the  $\{01\overline{1}3\}\langle 03\overline{3}2\rangle$  twins in the hcp lattice. In an elastic modelling approach as given here, the strain energy invariance forces us to include both twin systems or none of them, although they may display very different characteristics.

### References

- Abeyaratne, R. and Knowles, J. (2006). *Evolution of Phase Transitions A Continuum Theory* (Cambridge University Press).
- Al-Samman, T. and Gottstein, G. (2008). Room temperature formability of a magnesium AZ31 alloy: Examining the role of texture on the deformation mechanisms, *Materials Science and Engineering A* **488**, pp. 406–414.
- Bacon, D. and Liang, M. (1986). Computer simulation of dislocation cores in h.c.p. metals I. Interatomic potentials and stacking-fault stability, *Philosophical Magazine A* **53**, pp. 163–179.
- Ball, J. (1977). Convexity conditions and existence theorems in nonlinear elasticity, *Archive for Rational Mechanics and Analysis* **63**, pp. 337–403.
- Ball, J. and James, R. (1987). Fine phase mixtures as minimizers of energy, *Archive for Rational Mechanics and Analysis* **100**, pp. 13–52.
- Bartels, C., Carstensen, C., Hackl, K. and Hoppe, U. (2004). Effective relaxation for microstructure simulations: algorithms and applications, *Computer Methods in Applied Mechanics and Engineering* **193**, pp. 5143–5175.
- Bertram, A. (2003). Finite thermoplasticity based on isomorphisms, International Journal of Plasticity 19, pp. 2027–2050.
- Bingert, J., Mason, T., Kaschner, G., Maudlin, P. and Gray III, G. (2002). Deformation twinning in polycrystalline Zr: Insights from electron backscattered diffraction characterization, *Metallurgical and Materials Transactions A: Physical Metallurgy and Materials Science* 33, pp. 955–963.
- Böhlke, T., Bondár, G., Estrin, Y. and Lebyodkin, M. (2009). Geometrically non-linear modeling of the Portevin-Le Chatelier effect, *Computational Materials Science* 44, pp. 1076–1088.
- Carstensen, C., Hackl, K. and Mielke, A. (2002). Non-convex potentials and microstructures in finite-strain plasticity, *Proceedings of the Royal Society of London A* **458**, pp. 299–317.
- Chaboche, J., Feyel, F. and Monerie, Y. (2001). Interface debonding models: a viscous regularization with a limited rate dependency, *International Journal of Solids and Structures* **38**, pp. 3127–3160.
- Chino, Y., Kimura, K. and Mabuchi, M. (2008). Twinning behavior and deformation mechanisms of extruded az31 mg alloy, *Materials Science and Engineering A* **486**, pp. 481–488.
- Christian, J. and Mahajan, S. (1995). Deformation twinning, Progress in Materials Science 39, pp. 1–157.
- Dias da Silva, V. (2004). A simple model for viscous regularization of elasto-plastic constitutive laws with softening, *Communications in Numerical Methods in Engineering* **20**, pp. 547–568.
- Ericksen, J. (1975). Equilibrium of bars, Journal of Elasticity 5, pp. 191–202.
- Ericksen, J. (1984). Twinning of Crystals, *Preprint Series of the Institute for Mathematics and its Application of the University of Minnesota* **95**, pp. 1–18.
- Fisher, R. (1953). Dispersions on a sphere, Proceedings of the Royal Society of London A 217, pp. 295–305.
- Glüge, R., Bertram, A., Böhlke, T. and Specht, E. (2010). A Pseudoelastic Model for Mechanical Twinning on the Microscale, *Zeitschrift für Angewandte Mathematik und Mechanik, accepted for publication in the special issue "Phase Transitions in Deformable Solids and Structures"* DOI 10.1002/zamm.200900339.
- Govindjee, S., Mielke, A. and Hall, G. (2003). The free energy of mixing for n-variant martensitic phase transformations using quasi-convex analysis, *Journal of the Mechanics and Physics of Solids* **51**, pp. 1–26.
- Hartt, W. and Reed-Hill, R. (1968). Internal deformation and fracture of second-order  $\{10\overline{1}1\} \{10\overline{1}2\}$ -twins in magnesium, *Transactions of the metallurgical society of AIME* 242, pp. 1127–1133.
- Hou, T., Rosakis, P. and LeFloch, P. (1999). A Level-Set Approach to the Computation of Twinning and Phase-Transition Dynamics, *Journal of Computational Physics* **150**, pp. 302–331.
- Hutchinson, J. (1976). Bounds and self-consistent estimates for creep of polycrystalline materials, *Proceedings of the Royal Society of London A* **348**, pp. 101–127.
- Igarashi, M., Khantha, M. and Vitek, V. (1991). N-body potentials for hexagonal closed-packed metals, *Philosophical Magazine B* 63, pp. 603–627.
- Jiang, L., Jonas, J., Mishrab, R., Luob, A., Sachdevb, A. and Godetc, S. (2007). Twinning and texture development in two Mg alloys subjected to loading along three different strain paths, *Acta Materialia* **55**, pp. 3899–3910.
- Kelley, E. and Hosford, W. J. (1968). Plane-strain compression of magnesium and magnesium alloy crystals, *Transactions* of the Metallurgical Society of AIME **242**, pp. 5–13.

- Koike, J. (2005). Enhanced Deformation Mechanisms by Anisotropic Plasticity in Polycrystalline Mg Alloys at Room Temperature, *Metallurgical and Materials Transactions A* **36**, pp. 1689–1696.
- Lay, S. and Nouet, G. (1994). Interaction of slip dislocations with the (0112) twin interface in zinc, *Philosophical Magazine* A **70**, pp. 1027–1044.
- Li, B. and Ma, E. (2009a). Atomic shuffling dominated mechanism for deformation twinning in magnesium, *Physical Review Letters* **103**, pp. 35503–1–4.
- Li, B. and Ma, E. (2009b). Zonal dislocations mediating {1011} (1012) twinning in magnesium, *Acta Materialia* **57**, pp. 1734–1743.
- Li, H., Hsu, E., Szpunar, J., Verma, R. and Carter, J. (2007). Determination of Active Slip/Twinning Modes in AZ31 Mg Alloy Near Room Temperature, *Journal of Materials Engineering and Performance* **16**, 3, pp. 321–326.
- Markov, K. and Preziosi, L. (2000). *Heterogeneous Media: Micromechanics Modeling Methods and Simulations* (Birkhäuser, Boston).
- Meng, L., Yang, P., Xie, Q. and Mao, W. (2008). Analysis on compression twins in Magnesium, *Materials Transactions* **49**, pp. 710–714.
- Miehe, C. (2003). Computational micro-to-macro transition for discretized micro-structures of heterogeneous materials at finite strains based on the minimization of averaged incremental energy, *Computer Methods in Applied Mechanics and Engineering* **192**, pp. 559–591.
- Muránsky, O., Carr, D., Šittner, P. and Oliver, E. (2009). In situ neutron diffraction investigation of deformation twinning and pseudoelastic-like behaviour of extruded AZ31 magnesium alloy, *International Journal of Plasticity* 25, pp. 1107– 1127.
- Nemat-Nasser, S. (1999). Averaging theorems in finite deformation plasticity, *Mechanics of Materials* 31, pp. 493–523.
- Neumann, P. (1966). Vereinfachung kristallographischer Rechnungen in hexagonalen Gittern durch konsequente Benutzung des vierachsigen hexagonalen Koordinatensystems, *Physica Status Solidi* **17**, pp. K71–K74.
- Ortiz, M. and Repetto, E. (1999). Nonconvex energy minimization and dislocation structures in ductile single crystals, *Journal of the Mechanics and Physics of Solids* **47**, pp. 397–462.
- Pagano, S., Alart, P. and Maisonnueve, O. (1998). Solid-solid phase transition modelling. Local and global minimizations of non-convex and relaxed potentials. Isothermal case for shape memory alloys. *International Journal of Engineering Science* **36**, pp. 1143–1172.
- Partridge, P. (1965). Irregular Twin Growth and Contraction in Hexagonal Close Packed Metals, *Acta Metallurgica* 13, pp. 1330–1335.
- Pitteri, M. and Zanzotto, G. (2002). *Continuum Models for Phase Transitions and Twinning in Crystals* (Chapman and Hall/CRC).
- Reed-Hill, R. (1973). *The Inhomogeneity of Plastic Deformation*, chap. Role of Deformation Twinning in Determining the Mechanical Properties of Metals (American Society for Metals), pp. 285–311.

Reed-Hill, R. and Robertson, W. (1957a). Additional modes of deformation twinning in magnesium, *Acta Metallurgica* 5, pp. 717–727.

Reed-Hill, R. and Robertson, W. (1957b). The crystallographic characteristics of fracture in magnesium single crystals, *Acta Metallurgica* **5**, pp. 728–737.

- Roberts, E. and Partridge, P. (1966). The accommodation around  $\{10\overline{1}2\}\langle\overline{1}011\rangle$  twins in magnesium, *Acta Metallurgica* **14**, pp. 513–527.
- Roubíček, T. (2004). *Nonlinear Homogenization and its Applications to Composites, Polycrystals and Smart Materials,* chap. Models of Microstructure Evolution in Shape Memory Alloys (Kluwer Academic Publishers), pp. 269–304.
- Serra, A. and Bacon, D. (1986). Computer simulation of twin boundaries in the h.c.p. metals, *Philosophical Magazine A* **54**, pp. 793–804.
- Serra, A. and Bacon, D. (1991). Computer simulation of twinning dislocation in magnesium using a many-body potential, *Philosophical Magazine A* **63**, pp. 1001–1012.
- Serra, A. and Bacon, D. (1996). A new model for  $\{10\overline{1}2\}$  twin growth in hcp metals, *Philosophical Magazine A* 73, pp. 333–343.
- Sidi Ammi, M. and Torres, D. (2008). Regularity of Solutins of the Autonomous Integrals of the Calculus of Variations, in *Differential Equations, Chaos and Variational Problems* (Springer).

Simmons, G. and Wang, H. (1971). Single Crystal Elastic Constants and Calculated Aggregate Properties: A Handbook

(The M.I.T. Press).

- Simo, J. and Hughes, T. (1998). Computational Inelasticity (Springer-Verlag, New York).
- Stanford, N. (2008). Observation of {1121} twinning in a Mg-based alloy, *Philosophical Magazine Letters* **88**, pp. 379–386.
- Suquet, P. (1987). *Homogenization Techniques for Composite Media, Lecture Notes in Physics Vol.* 272, chap. Elements of Homogenization for Inelastic Solid Mechanics (Springer Verlag, New York), pp. 193–278.
- Ungár, T., Glavicic, M., Balogh, L., Nyilas, K., Salem, A., Ribárik, G. and Semiatin, S. (2008). The use of X-ray diffraction to determine slip and twinning activity in commercial-purity (CP) titanium, *Materials Science and Engineering A* **493**, pp. 79–85.
- Wang, Y. and Huang, J. (2007). The role of twinning and untwinning in yielding behavior in hot-extruded Mg-Al-Zn alloy, *Acta Materialia* **55**, 3, pp. 897–905.
- Wang, Y., Jin, Y. and Khachaturyan, A. (2004). The Effects of Free Surfaces on Martensite Microstructures: 3D Phase Field Microelasticity Simulation Study, *Acta Materialia* **52**, 4, pp. 1039–1050.
- Wonsiewicz, B. and Backofen, W. (1967). Plasticity of magnesium crystals, *Transactions of the metallurgical society of AIME* 239, pp. 1422–1431.
- Yi, S., Schestakow, I. and Zaefferer, S. (2009). Twinning-related microstructural evolution durcing hot rolling and subsequent annealing of pure magnesium, *Materials Science and Engineering A* **516**, pp. 58–64.
- Yin, S., Yang, F., Yang, X., Wu, S., Li, S. and Li, G. (2008). The role of twinning-detwinning on fatigue fracture morphology of Mg-3%Al-1%Zn alloy, *Materials Science and Engineering A* **494**, pp. 397–400.
- Zhou, A., Basu, S. and Barsoum, M. (2008). Kinking nonlinear elasticity, damping and microyielding of hexagonal closepacked metals, *Acta Materialia* 56, pp. 60–67.
- Zimmer, J. (2006). Jog my shape memory: dynamics as a challenge in mathematical materials science, *Philosophical Transactions of the Royal Society of London A* **364**, pp. 3285–3300.
- Zohdi, T. and Wriggers, P. (2001). Computational Micro-macro Material Testing, *Archives of Computational Methods in Engineering* **8**, 2, pp. 131–228.